A variable switching point predictive current control strategy for quasi-Z-source inverters

A Variable Switching Point Predictive Current Control Strategy for Quasi-Z-Source Inverters

Petros Karamanakos, *Member, IEEE*, Ayman Ayad, *Member, IEEE*, and Ralph Kennel, *Senior Member, IEEE*

***Abstract*—This paper presents a variable switching point predictive current control (VSP^{2}CC) for the quasi-Z-source inverter (qZSI). The proposed VSP^{2}CC aims to remove the output current error on the ac side as well as the inductor current and capacitor voltage errors of the quasi-Z-source network on the dc side of the converter. Unlike the previously presented direct model predictive control (MPC) strategies for the qZSI, the proposed control scheme can directly apply the switching signals not only at the discrete time instants, but at any time instant within the sampling interval. Consequently, the shoot-through state can be applied for a shorter time than the sampling interval, resulting in lower output and inductor currents ripples. Experimental results based on an FPGA are provided to verify the effectiveness of the introduced control method. As it is shown, the proposed method leads to lower inductor current ripples and less output current total harmonic distortion (THD) when compared with the conventional direct MPC.**

***Index Terms*—Model predictive control (MPC), variable switching point (VSP), quasi-Z-source inverter (qZSI), current control**

I. Introduction

THE Z-source inverter (ZSI) has been proposed as an effective alternative to the conventional voltage source inverter (VSI) [2]–[4]. The ZSI utilizes an impedance network, consisting of two identical inductors and two identical capacitors, in order to boost the input dc voltage to the desired dc-link level. This is achieved by introducing a shoot-through state, according to which at least one of the inverter legs is short-circuited [2]. Besides the boosting functionality of the shoot-through state, allowing for short-circuited phases implies that the dead time required with the conventional VSIs is not an issue for the ZSI. As a result, the output current/voltage distortions decrease and a high inverter reliability is reached [5], [6].

More recently, the quasi-Z-source inverter (qZSI) was introduced as an improved version of the ZSI [7]. Thanks to its extra advantages, such as continuous input current, smaller passive components, and common ground point between the input and the dc-link bus, the qZSI has been used in a wide range of applications, such as general-purpose variable speed drives [8], electric vehicles [9], [10], distributed generation applications [11], applications with battery energy storage units [12], and photovoltaic power systems [13], [14].

The qZSI can been considered as a buck-boost converter since it performs the functions of a dc-dc and dc-ac converter in one single stage. This implies that two decoupled controllers are required to fully control the system; one for the dc, and one for the ac side. More specifically, the dc-side controller adjusts the capacitor voltage (dc-link voltage) by controlling the shoot-through duty cycle, whereas the ac-side controller manipulates the inverter modulation index to regulate the output ac current/voltage to the desired value. To this end, conventional linear controllers, such as proportional-integral (PI) controllers, are utilized and combined with a pulse width modulation (PWM) stage to generate the switching signals [9], [11], [14]–[16]. Although such controllers have exhibited satisfactory performance, the design process is cumbersome since additional anti-windup mechanisms and rate limiters are required as well as cascaded control loops need to be designed for both sides of the converter, see [16] and references therein.

As an alternative, *direct* model predictive control (MPC), also referred to as finite control set MPC (FCS-MPC), has been recently applied to the qZSI [17]–[24]. Thanks to its fast dynamic response, implementation simplicity and ability to handle multiple control objectives [25]–[33], MPC has proved to be an effective control algorithm for the qZSI. With direct MPC the control objectives—i.e., the regulation of the output current, inductor current, and capacitor voltage to their reference values as well as control of the switching frequency—are mapped into an objective function which is minimized in real time in order to conclude to the optimal control action (i.e., the switches position) that results in the best possible system behavior. Subsequently, the computed optimal switches position is directly fed to the converter, thus a modulation stage is bypassed. That way, the same switches position is applied to the system for at least one sampling interval, meaning that the converter can operate at the shoot-though state for long time intervals. Given that this phenomenon is further aggravated when the converter operates at low switching frequencies, the resulting inductor current ripples and output current total harmonic distortion (THD) can be fairly high [24].

As a workaround to this inherent problem of direct MPC, some techniques have been proposed that include a "modulator" to the control scheme, with an eventual goal to reduce the ripples of the variables of interest, depending on the examined case study (e.g., output current, electromagnetic torque, flux, etc.) [34]–[44]. This is done by introducing as an additional optimization variable to the direct MPC problem the

A preliminary version of this paper was presented at the *IEEE Applied Power Electronics Conference and Exposition*, Tampa, FL, 2017, see [1].

P. Karamanakos is with the Faculty of Computing and Electrical Engineering, Tampere University of Technology, Tampere 33101, Finland; e-mail: p.karamanakos@ieee.org

A. Ayman and R. Kennel are with the Chair of Electrical Drive Systems and Power Electronics, Technische Universität München, Munich 80333, Germany; e-mail: ayman.francees@tum.de; ralph.kennel@tum.de

time instant within the sampling interval the optimal switches position should be applied to the converter in order for the ripples of the variables of concern to be minimized. In other words, such schemes allow for the converter switches to change state not only at the discrete time instants, but also at any instant within the sampling interval. Consequently, the switches positions that can potentially lead to high ripples are applied for less time than with conventional direct MPC schemes, resulting in an overall improved system performance.

Motivated by the advantages of the aforementioned approaches, this paper proposes a variable switching point predictive current control (VSP^{2}CC) for the qZSI. In addition to the above-mentioned control objectives for the qZSI, the proposed scheme aims to reduce the output and inductor currents ripples by changing the switches position at any time instant within the sampling interval, thus, reducing the time of operation at the shoot-through state. The introduced method is implemented on a low-cost field programmable gate array (FPGA) Cyclone III-EP3C40Q240C8 and its performance is experimentally investigated with a qZSI and an RL load. As shown, the presented control algorithm results in lower inductor current ripples and output current THD compared with the conventional direct MPC when operating the converter at the same switching frequency.

This paper is structured as follows. Section II introduces the mathematical model of the qZSI. The proposed VSP^{2}CC strategy is presented and analyzed in Section III. In Section IV, experimental results are provided and discussed. Finally, the conclusions are drawn in Section V.

II. Physical Model of the Quasi-Z-Source Inverter

Before proceeding with the system modeling, it should be noted that in order to simplify the derivations of both the mathematical description of the system and the optimal control problem, any variable in the three-phase abc-plane, i.e., $\boldsymbol{\xi}_{abc} = [\xi_a \ \xi_b \ \xi_c]^T$ is transformed to a two-dimensional variable $\boldsymbol{\xi}_{\alpha\beta} = [\xi_\alpha \ \xi_\beta]^T$ in the stationary, orthogonal $\alpha\beta$-plane, via the transformation matrix $\boldsymbol{K}$, i.e., $\boldsymbol{\xi}_{\alpha\beta} = \boldsymbol{K}\boldsymbol{\xi}_{abc}$,[1] where $\boldsymbol{K}$ is the Clarke transformation matrix

$$\boldsymbol{K} = \frac{2}{3}\begin{bmatrix} 1 & -\frac{1}{2} & -\frac{1}{2} \\ 0 & \frac{\sqrt{3}}{2} & -\frac{\sqrt{3}}{2} \end{bmatrix}. \tag{1}$$

A. Continuous-Time Model

The system under discussion, consisting of a quasi-Z-source (qZS) network, a two-level three-phase inverter, and an RL load, is shown in Fig. 1. Depending on the switches position, the qZSI can operate at two different states, i.e., the non-shoot-through and the shoot-through state. When operating at the former state (Fig, 2(a)), the dc-ac part of the converter operates as the conventional two-level VSI, i.e., it can produce eight voltage vectors, six of which are active and two zero [45]. Operation at the latter state means that at least one phase leg

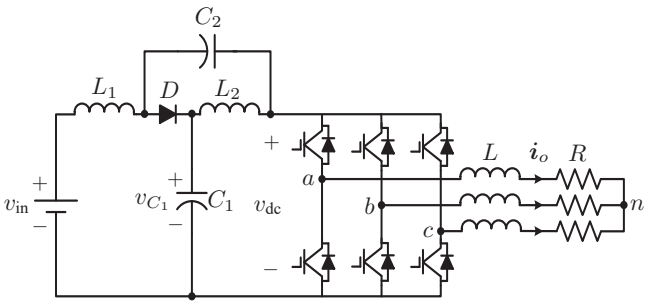

Fig. 1: Topology of the quasi-Z-source inverter (qZSI).

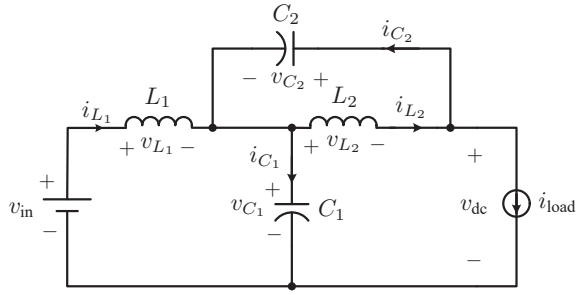

(a) Non-shoot-through state.

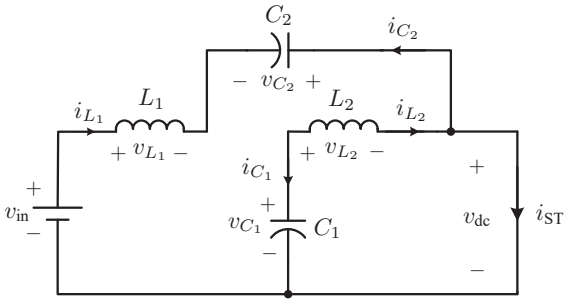

(b) Shoot-through state (i_{ST} stands for the shoot-through current, i.e., the dc-link current during the shoot-through state).

Fig. 2: Operational states of the qZSI.

of the inverter is short circuited (both switches of the same phase are simultaneously on); the resulting equivalent circuit is presented in Fig. 2(b). Consequently, in order to derive an accurate model of the converter that will serve as an internal prediction model for the VSP^{2}CC, the two operating states will be examined first separately and, following, the overall model of the system will be obtained.

To fully describe the dynamics of the qZSI, the output current, the inductor currents, and the capacitor voltages are chosen as state variables. Therefore, the state vector is of the form

$$\boldsymbol{x} = \begin{bmatrix} i_{o,\alpha} & i_{o,\beta} & i_{L_1} & i_{L_2} & v_{C_1} & v_{C_2} \end{bmatrix}^T \in \mathbb{R}^6. \tag{2}$$

The output and the inductor currents as well as the capacitor voltage constitute the output vector[2], i.e., $\boldsymbol{y} = [i_{o,\alpha} \ i_{o,\beta} \ i_{L_1} \ v_{C_1}]^T \in \mathbb{R}^4$. Moreover, the system

[1] Throughout the paper, for vectors in the abc-plane the corresponding subscript is dropped for notational simplicity. Vectors in the $\alpha\beta$-plane, however, are denoted with the corresponding subscript.

[2] Due to the symmetry of the qZS network, only one inductor current and one capacitor voltage are considered as output variables.

input is the switches position $\boldsymbol{u} \in \boldsymbol{\mathcal{U}} = \mathcal{U}^3$ with

$$\boldsymbol{u} = \begin{bmatrix} u_a & u_b & u_c \end{bmatrix}^T . \tag{3}$$

The integer variable $u_\zeta \in \mathcal{U}$ in (3), with $\zeta \in \{a, b, c\}$, denotes the switch position in phase ζ, and it is constrained to the set

$$\mathcal{U} = \{0, 1\} . \tag{4}$$

Finally, the input dc voltage is considered as a disturbance to the system, i.e., $\boldsymbol{w} = v_{\text{in}} \in \mathbb{R}$.

1) Non-Shoot-Through State: During the non-shoot-through state, as shown in Fig. 2(a), the input voltage source and the inductors charge the capacitors and feed the load. Accordingly, the converter model is obtained by

$$\frac{\mathrm{d}\boldsymbol{x}(t)}{\mathrm{d}t} = \boldsymbol{F}_1 \boldsymbol{x}(t) + \boldsymbol{G}_1 \boldsymbol{u}(t) + \boldsymbol{H}\boldsymbol{w}(t) \tag{5a}$$

$$\boldsymbol{y}(t) = \boldsymbol{E}\boldsymbol{x}(t) , \tag{5b}$$

where[3]

$$\boldsymbol{F}_1 = \begin{bmatrix} -\frac{R}{L} & 0 & 0 & 0 & 0 & 0 \\ 0 & -\frac{R}{L} & 0 & 0 & 0 & 0 \\ 0 & 0 & 0 & 0 & -\frac{1}{L_1} & 0 \\ 0 & 0 & 0 & 0 & 0 & -\frac{1}{L_2} \\ -\frac{\boldsymbol{u}^T \boldsymbol{K}^{-1}_{(:,1)}}{C_1} & -\frac{\boldsymbol{u}^T \boldsymbol{K}^{-1}_{(:,2)}}{C_1} & \frac{1}{C_1} & 0 & 0 & 0 \\ -\frac{\boldsymbol{u}^T \boldsymbol{K}^{-1}_{(:,1)}}{C_2} & -\frac{\boldsymbol{u}^T \boldsymbol{K}^{-1}_{(:,2)}}{C_2} & 0 & \frac{1}{C_2} & 0 & 0 \end{bmatrix} ,$$

$$\boldsymbol{G}_1 = \hat{v}_{\text{dc}} \begin{bmatrix} \frac{1}{L} & 0 \\ 0 & \frac{1}{L} \\ 0 & 0 \\ 0 & 0 \\ 0 & 0 \\ 0 & 0 \end{bmatrix} \boldsymbol{K}, \ \boldsymbol{H} = \begin{bmatrix} 0 \\ 0 \\ \frac{1}{L_1} \\ 0 \\ 0 \\ 0 \end{bmatrix} ,$$

$$\boldsymbol{E} = \begin{bmatrix} 1 & 0 & 0 & 0 & 0 & 0 \\ 0 & 1 & 0 & 0 & 0 & 0 \\ 0 & 0 & 1 & 0 & 0 & 0 \\ 0 & 0 & 0 & 0 & 1 & 0 \end{bmatrix} ,$$

with R (L) being the load resistance (inductance), and $\hat{v}_{\text{dc}}$ the peak dc-link voltage, see the appendix.

2) Shoot-Through State: As can be seen in Fig. 2(b), the diode is reverse biased and the load is short-circuited when the converter operates at the shoot-through state. During this operation the input voltage source and the capacitors charge the inductors. Consequently, the model is given by

$$\frac{\mathrm{d}\boldsymbol{x}(t)}{\mathrm{d}t} = \boldsymbol{F}_2 \boldsymbol{x}(t) + \boldsymbol{G}_2 \boldsymbol{u}(t) + \boldsymbol{H}\boldsymbol{w}(t) \tag{6a}$$

$$\boldsymbol{y}(t) = \boldsymbol{E}\boldsymbol{x}(t) , \tag{6b}$$

[3]For a matrix $\boldsymbol{M}$, $\boldsymbol{M}_{(:,i)}$ denotes its ith column.

where

$$\boldsymbol{F}_2 = \begin{bmatrix} -\frac{R}{L} & 0 & 0 & 0 & 0 & 0 \\ 0 & -\frac{R}{L} & 0 & 0 & 0 & 0 \\ 0 & 0 & 0 & 0 & 0 & \frac{1}{L_1} \\ 0 & 0 & 0 & 0 & \frac{1}{L_2} & 0 \\ 0 & 0 & 0 & -\frac{1}{C_1} & 0 & 0 \\ 0 & 0 & -\frac{1}{C_2} & 0 & 0 & 0 \end{bmatrix} ,$$

and $\boldsymbol{G}_2$ is the zero matrix of appropriate dimensions. It is worthwhile to point out that the latter implies that the qZSI at this state of operation can be considered as an autonomous linear dynamical system with an external disturbance.

3) Complete Model of the System: The derived models (5) and (6) can be integrated into one model that precisely describes the dynamics of the converter when operating at the different states. To this aim, an auxiliary binary variable d_{aux} is introduced. This variable indicates the state at which the converter operates, i.e.,

$$d_{\text{aux}} = \begin{cases} 0 & \text{if non-shoot-through state} \\ 1 & \text{if shoot-through state} \end{cases} . \tag{7}$$

The transition from non-shoot-through state to shoot-through state, and vice versa, is input-dependent, thus (7) can be written as

$$d_{\text{aux}} = \begin{cases} 0 & \text{if } u_\zeta \neq \bar{u}_\zeta \forall\, \zeta \in \{a, b, c\} \\ 1 & \text{if } \exists \zeta \in \{a, b, c\} \text{ s.t. } u_\zeta = \bar{u}_\zeta = 1 \end{cases} , \tag{8}$$

where $\bar{u}_\zeta$ denotes the position of the lower switch in phase ζ.

Taking all the above into account, the model of the converter can be written as

$$\frac{\mathrm{d}\boldsymbol{x}(t)}{\mathrm{d}t} = \boldsymbol{F}\boldsymbol{x}(t) + \boldsymbol{G}\boldsymbol{u}(t) + \boldsymbol{H}\boldsymbol{w}(t) \tag{9a}$$

$$\boldsymbol{y}(t) = \boldsymbol{E}\boldsymbol{x}(t) , \tag{9b}$$

where

$$\boldsymbol{F} = \begin{bmatrix} -\frac{R}{L} & 0 & 0 & 0 & 0 & 0 \\ 0 & -\frac{R}{L} & 0 & 0 & 0 & 0 \\ 0 & 0 & 0 & 0 & \frac{d_{\text{aux}}-1}{L_1} & \frac{d_{\text{aux}}}{L_1} \\ 0 & 0 & 0 & 0 & \frac{d_{\text{aux}}}{L_2} & \frac{d_{\text{aux}}-1}{L_2} \\ \frac{m_1}{C_1} & \frac{m_2}{C_1} & \frac{1-d_{\text{aux}}}{C_1} & -\frac{d_{\text{aux}}}{C_1} & 0 & 0 \\ \frac{m_1}{C_2} & \frac{m_2}{C_2} & -\frac{d_{\text{aux}}}{C_2} & \frac{1-d_{\text{aux}}}{C_2} & 0 & 0 \end{bmatrix} ,$$

with m_1 and m_2 being

$$m_1 = (d_{\text{aux}} - 1)\boldsymbol{u}^T \boldsymbol{K}^{-1}_{(:,1)} ,$$
$$m_2 = (d_{\text{aux}} - 1)\boldsymbol{u}^T \boldsymbol{K}^{-1}_{(:,2)} ,$$

respectively, and $\boldsymbol{G} = (1 - d_{\text{aux}})\boldsymbol{G}_1$.

In Fig. 3 the operating states of the converter are described, where the qZSI is represented as an automaton [24]. The condition that specifies the transitions from one state to another is given by the auxiliary variable d_{aux} which depends on the single-phase switch position, see (8).

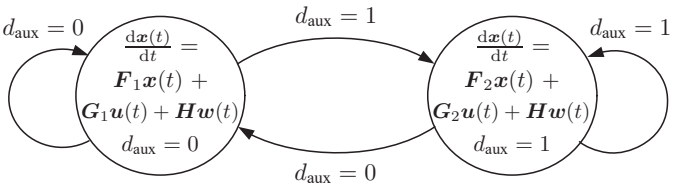

Fig. 3: The qZSI presented as an automaton driven by conditions.

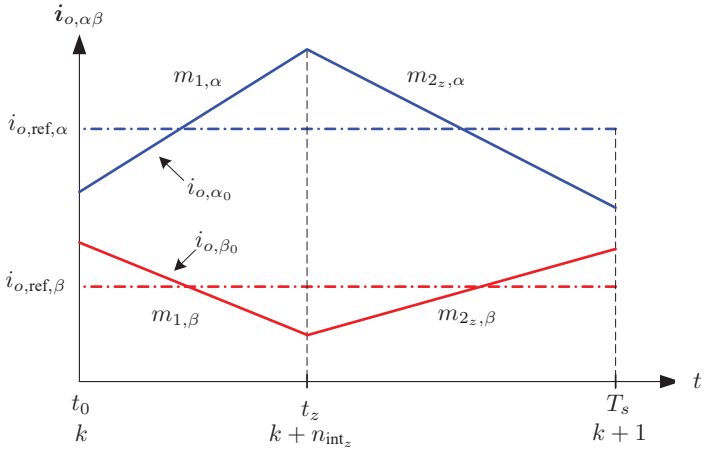

Fig. 4: Concept of the variable switching point.

B. Prediction Model

To compute the predictions of the variables of interest, the discrete-time model of the qZSI is required. Hence, by using forward Euler approximation, the continuous-time model (9) is discretized as follows

$$\boldsymbol{x}(k+1) = \boldsymbol{A}\boldsymbol{x}(k) + \boldsymbol{B}\boldsymbol{u}(k) + \boldsymbol{D}\boldsymbol{w}(k) \tag{11a}$$

$$\boldsymbol{y}(k) = \boldsymbol{C}\boldsymbol{x}(k), \tag{11b}$$

where $\boldsymbol{A} = \boldsymbol{F}T_s + \boldsymbol{I}$, $\boldsymbol{B} = \boldsymbol{G}T_s$, $\boldsymbol{D} = \boldsymbol{H}T_s$ and $\boldsymbol{C} = \boldsymbol{E}$. Moreover, $\boldsymbol{I}$ is the identity matrix of appropriate dimensions, T_s denotes the sampling interval, and $k \in \mathbb{N}$.

III. Variable Switching Point Predictive Current Control Strategy

A. Control Objectives

The main control goal of the proposed VSP^{2}CC strategy is to regulate the output current, inductor current, and capacitor voltage along their reference values by appropriately manipulating the switches position. An additional objective is to keep the switching frequency relatively low in order to reduce the switching losses. Moreover, the output current ripples are to be minimized. To achieve these goals, the control algorithm not only computes the optimal switches position that meets the aforementioned tasks, but also it calculates the time instant—referred to as variable switching point (VSP)—at which it should be applied to the converter.

B. Proposed Control Algorithm

Let $\boldsymbol{u}_z$, with $z \in \{0, 1, \cdots, 7\}$, denote the candidate switches position that is to be applied at the time instant (i.e., VSP)

$$t_z = n_{\text{int}_z}^{(k)} T_s \in [0, T_s)\ , \tag{12}$$

with $n_{\text{int}_z}^{(k)} \in [0, 1)$ being the normalized time instant between the time-steps k and $k+1$.[4] The goal of the proposed algorithm is to compute that pair $\boldsymbol{U}(k) = (\boldsymbol{u}_z, t_z)$ that meets the objectives mentioned in Section III-A. To do so, the possible VSPs t_z need to be computed for all candidate switches positions $\boldsymbol{u}_z$; this is done by considering the ripple of the output current.

More specifically, minimization of the output current ripples can be interpreted as minimization of the energy content of the output current error $\boldsymbol{i}_{o,\text{err},\alpha\beta} = \boldsymbol{i}_{o,\text{ref},\alpha\beta} - \boldsymbol{i}_{o,\alpha\beta}$, where $\boldsymbol{i}_{o,\text{ref},\alpha\beta}$ is the reference value of the output current. This implies that for the calculation of the VSP t_z the (squared) rms value of the output current error needs to be minimized. To simplify the computation, since $T_s \ll T_0$, where T_s is the sampling interval and T_0 the fundamental period, it can be assumed that the output current evolves linearly (as can be also deduced from (11)) within one T_s. For the same reason, it can be assumed that the current reference remains constant within the same time interval. Fig. 4 shows the evolution of the output current within one T_s when one of the candidate switches positions $\boldsymbol{u}_z$ is applied, i.e., only for one of the eight possible pairs $(\boldsymbol{u}_z, t_z)$. As can be seen, the switches position $\boldsymbol{u}(k)$ is applied to the converter for the interval $[0, t_z)$ and the current evolves with constant slope $\boldsymbol{m}_{1,\alpha\beta}$. For the remaining time (i.e., $[t_z, T_s)$), the candidate switches position $\boldsymbol{u}_z$ is implemented, and the current changes linearly with slope $\boldsymbol{m}_{2_z,\alpha\beta}$.

Given the above, the (squared) rms value of the output current error is given by[5]

$$i^2_{o,\text{err,rms},\alpha\beta}(t_z) = \frac{1}{T_s}\Bigg(\int_0^{t_z} ||\boldsymbol{i}_{o,\text{ref},\alpha\beta}(k) - \boldsymbol{i}_{o,\alpha\beta}(t, \boldsymbol{u}(k))||_2^2 \,\mathrm{d}t + \int_{t_z}^{T_s} ||\boldsymbol{i}_{o,\text{ref},\alpha\beta}(k) - \boldsymbol{i}_{o,\alpha\beta}(t, \boldsymbol{u}_z(k + n_{\text{int}_z}^{(k)}))||_2^2 \,\mathrm{d}t \Bigg), \tag{13}$$

with $\boldsymbol{i}_{o,\alpha\beta}(t, \boldsymbol{u}(k))$ and $\boldsymbol{i}_{o,\alpha\beta}(t, \boldsymbol{u}(k + n_{\text{int}_z}^{(k)}))$ being the output currents resulting from the applied switches position $\boldsymbol{u}(k)$ and candidate switches positions $\boldsymbol{u}_z$, respectively, given by

$$\boldsymbol{i}_{o,\alpha\beta}(t, \boldsymbol{u}(k)) = \boldsymbol{m}_{1,\alpha\beta} \cdot t + \boldsymbol{i}_{o,\alpha\beta}(t_0)\ ,\ t \in [0, t_z)\ , \tag{14}$$

and

$$\boldsymbol{i}_{o,\alpha\beta}(t, \boldsymbol{u}(k + n_{\text{int}_z}^{(k)})) = \boldsymbol{m}_{2_z,\alpha\beta} \cdot t + \boldsymbol{i}_{o,\alpha\beta}(t, \boldsymbol{u}(k))\ ,\ t \in [t_z, T_s), \tag{15}$$

where $\boldsymbol{i}_{o,\alpha\beta}(t_0) \equiv \boldsymbol{i}_{o,\alpha\beta}(k)$ in (14) stands for the measured output current.

Regarding the current slope $\boldsymbol{m}_{1,\alpha\beta}$ (see (14)), this is computed by considering that the switches position $\boldsymbol{u}^*(k - 1 + n_{\text{int}}^{*(k-1)})$ applied at time instant $(k - 1 + n_{\text{int}}^{*(k-1)})T_s$—i.e., in the previous sampling interval—is also applied at time-step k, i.e., $\boldsymbol{u}(k) = \boldsymbol{u}^*(k - 1 + n_{\text{int}}^{*(k-1)})$. Then, by using the system

[4]Note that positions $\boldsymbol{u}_0$ to $\boldsymbol{u}_6$ correspond to the seven unique voltage vectors present in the non-shoot-through state ($d_{\text{aux}} = 0$), with $\boldsymbol{u}_0$ corresponding the zero vector (i.e., $\boldsymbol{u}_0 = [0\ 0\ 0]^T$ or $\boldsymbol{u}_0 = [1\ 1\ 1]^T$), and $\boldsymbol{u}_1, \ldots \boldsymbol{u}_6$ corresponding to the six active vectors. Position $\boldsymbol{u}_7$ is the switch combination that leads to the shoot-through state ($d_{\text{aux}} = 1$).

[5]Note that the rms value of the output current error is a scalar.

model (11) and the measured output current $\boldsymbol{i}_{o,\alpha\beta}(k)$, the predicted output current at step $k+1$, i.e., $\boldsymbol{i}_{o,\alpha\beta}(k+1)$, is computed. Hence, $\boldsymbol{m}_{1,\alpha\beta}$ is given by

$$\boldsymbol{m}_{1,\alpha\beta} = \frac{\boldsymbol{i}_{o,\alpha\beta}(k+1)|_{\boldsymbol{u}(k)=\boldsymbol{u}^*(k-1+n_{\text{int}}^{*(k-1)})} - \boldsymbol{i}_{o,\alpha\beta}(k)}{T_s}. \tag{16}$$

As for the eight possible current slopes $\boldsymbol{m}_{2_z,\alpha\beta}$, they are calculated by computing the predicted output current $\boldsymbol{i}_{o,\alpha\beta}(k+1)$ under the assumption that the switches position at time-step k can be anyone of the eight possibilities (i.e., $\boldsymbol{u}(k) = \boldsymbol{u}_z$). Therefore, the possible current slopes $\boldsymbol{m}_{2_z,\alpha\beta}$ are

$$\boldsymbol{m}_{2_z,\alpha\beta} = \frac{\boldsymbol{i}_{o,\alpha\beta}(k+1)|_{\boldsymbol{u}(k)=\boldsymbol{u}_z} - \boldsymbol{i}_{o,\alpha\beta}(k)}{T_s}. \tag{17}$$

After computing the current slopes $\boldsymbol{m}_{1,\alpha\beta}$ (16) and $\boldsymbol{m}_{2_z,\alpha\beta}$ (17) the VSPs can be derived by minimizing (13). This is done by setting the derivative of the (squared) rms value of the output current error equal to zero, i.e.,

$$\frac{\mathrm{d}i^2_{o,\text{err,rms},\alpha\beta}(t_z)}{\mathrm{d}t_z} = 0\,. \tag{18}$$

This yields

$$t_z = \frac{p}{q} \tag{19}$$

where

$$p = (2\boldsymbol{i}_{o,\alpha\beta}(k) - 2\boldsymbol{i}_{o,\text{ref},\alpha\beta}(k) + T_s\boldsymbol{m}_{2_z,\alpha\beta})^T(\boldsymbol{m}_{2_z,\alpha\beta} - \boldsymbol{m}_{1,\alpha\beta})$$

and

$$q = (2\boldsymbol{m}_{1,\alpha\beta} - \boldsymbol{m}_{2_z,\alpha\beta})^T(\boldsymbol{m}_{1,\alpha\beta} - \boldsymbol{m}_{2_z,\alpha\beta})\,.$$

Having found the possible VSPs, the evolution of the output variables is computed over two different time intervals, i.e., $[0, t_z)$ and $[t_z, T_s)$. More specifically, the value of the output vector $\boldsymbol{y}$ at step $k + n_{\text{int}_z}^{(k)}$ is computed based on (11) and the pair $(\boldsymbol{u}(k), t_z)$, where $\boldsymbol{u}(k)$ is the previously applied solution. Following, (11) is used to compute $\boldsymbol{y}(k+1)$ for each one of the derived pairs $(\boldsymbol{u}_z, t_z)$, with the difference that the prediction is done over the time interval $T_s - t_z$.

With all information required available (i.e., the values of $\boldsymbol{y}(k+n_{\text{int}_z}^{(k)})$ and $\boldsymbol{y}(k+1)$) an objective function is formulated in order to map the control objectives, as stated in Section III-A, into a scalar. The function is of the form

$$J(k) = \sum_{\xi\in\mathcal{S}} \Big(||\boldsymbol{y}_{\text{ref}} - \boldsymbol{y}(k+\xi|k)||^2_{\boldsymbol{Q}} \Big) + \lambda_u ||\Delta\boldsymbol{u}(k|k)||_2^2\,, \tag{20}$$

where $\boldsymbol{y}_{\text{ref}} = [i_{o,\text{ref},\alpha} \;\; i_{o,\text{ref},\beta} \;\; i_{L_1,\text{ref}} \;\; v_{C_1,\text{ref}}]^T$ and $\mathcal{S} = \Big\{ n_{\text{int}_z}^{(k)},\, 1 \Big\}$. The second term in (20), with $\Delta\boldsymbol{u}(k) = \boldsymbol{u}(k+1) - \boldsymbol{u}(k)$,[6] is added to adjust the switching frequency of the converter by penalizing changes in the manipulated variable. The weighting factor $\lambda_u > 0$ and the diagonal positive semidefinite weighting matrix[7] $\boldsymbol{Q} \in \mathbb{R}^{4\times4}$ are added to adjust the trade-off between the tracking performance and the converter switching frequency.

More specifically, as far as the tracking performance of the converter is concerned, the diagonal entries of $\boldsymbol{Q}$ set the priority between the tracking accuracy among the three output variables. Since for low current distortions the output current ripple needs to be much smaller than the input current and capacitor voltage ripples [32], priority is given to that by choosing larger values for the weighting factors of the α- and β-components of the output current. Thus, the first two diagonal entries of $\boldsymbol{Q}$ are of greater value compared with the other two. This implies that, in effect, the ratio between $\boldsymbol{Q}$ and λ_u decides on the—simplified—trade-off between the output current THD and the switching frequency of the converter. The latter is computed according to

$$f_{\text{sw}} = \lim_{M\to\infty} \frac{1}{MT_s} \cdot \frac{1}{6} \sum_{\ell=0}^{M-1} \frac{1}{2} \Big(||\boldsymbol{u}(\ell) - \boldsymbol{u}(\ell-1)||_1 + ||\bar{\boldsymbol{u}}(\ell) - \bar{\boldsymbol{u}}(\ell-1)||_1 \Big)\,. \tag{21}$$

i.e., by counting the number of *on* switching commutations over a time interval of length MT_s and by dividing this number by the length of that interval. By doing so, the switching frequency for each of the 6 controllable switches of the qZSI is found. Following, the average value of the aforementioned frequencies is calculated to yield the *average* switching frequency. It is important to point out that the first term of the summation in (21), i.e., $||\boldsymbol{u}(\ell) - \boldsymbol{u}(\ell-1)||_1$, does not suffice to provide an accurate value for the switching frequency. The reason is that—in contrast to the conventional VSI—the switches in phase $\zeta \in \{a, b, c\}$ are not necessarily turned on and off in a complementary manner, i.e., when the upper switch is on the lower is off ($u_\zeta = 1 \to \bar{u}_\zeta = 0$), and vice versa ($u_\zeta = 0 \to \bar{u}_\zeta = 1$); when the converter operates at shoot-through state they can be simultaneously on ($u_\zeta = 1$ and $\bar{u}_\zeta = 1$). To take this case into account the term $||\bar{\boldsymbol{u}}(\ell) - \bar{\boldsymbol{u}}(\ell-1)||_1$, with $\bar{\boldsymbol{u}} = [\bar{u}_a \;\; \bar{u}_b \;\; \bar{u}_c]^T$, is added to the expression. Since the introduction of the second term, however, results in counting each switching commutation twice, the final result is divided by 2.

Subsequently, the optimal switches position and the corresponding VSP, i.e., the pair $\boldsymbol{U}^*(k) = (\boldsymbol{u}^*, t^*)$, are found by solving the following optimization problem in real time

$$\begin{aligned}
\underset{\boldsymbol{U}(k)}{\text{minimize}} \quad & J(k) \\
\text{subject to} \quad & \boldsymbol{x}(\ell_1) = \boldsymbol{A}\boldsymbol{x}(\ell_2) + \boldsymbol{B}\boldsymbol{u}(\ell_2) + \boldsymbol{D}\boldsymbol{w}(\ell_2) \\
& \boldsymbol{y}(\ell_1) = \boldsymbol{C}\boldsymbol{x}(\ell_1) \\
& (\ell_1, \ell_2) \in \big\{ (k + n_{\text{int}_z}^{(k)}, k), (k+1, k+n_{\text{int}_z}^{(k)}) \big\} \\
& \boldsymbol{U}(k) \in \big\{ (\boldsymbol{u}_0, t_0), \ldots, (\boldsymbol{u}_7, t_7) \big\} \\
& \boldsymbol{u}(\ell_2) \in \mathcal{U} \\
& t_z \in [0, T_s)\,.
\end{aligned} \tag{22}$$

In a last step, a "modulator"—that operates at a higher sampling frequency than the MPC algorithm, i.e., $T_s' = T_s/m$, $m \in \mathbb{N}^+$—is used to apply the optimal switches position $\boldsymbol{u}^*$

[6] As explained in this section, it holds that $\boldsymbol{u}^*(k-1+n_{\text{int}}^{*(k-1)}) = \boldsymbol{u}(k)$ and $\boldsymbol{u}_z(k+n_{\text{int}_z}^{(k)}) = \boldsymbol{u}(k+1)$.

[7] The squared norm weighted with the positive (semi)definite matrix $\boldsymbol{W}$ is given by $||\boldsymbol{\xi}||^2_{\boldsymbol{W}} = \boldsymbol{\xi}^T\boldsymbol{W}\boldsymbol{\xi}$.

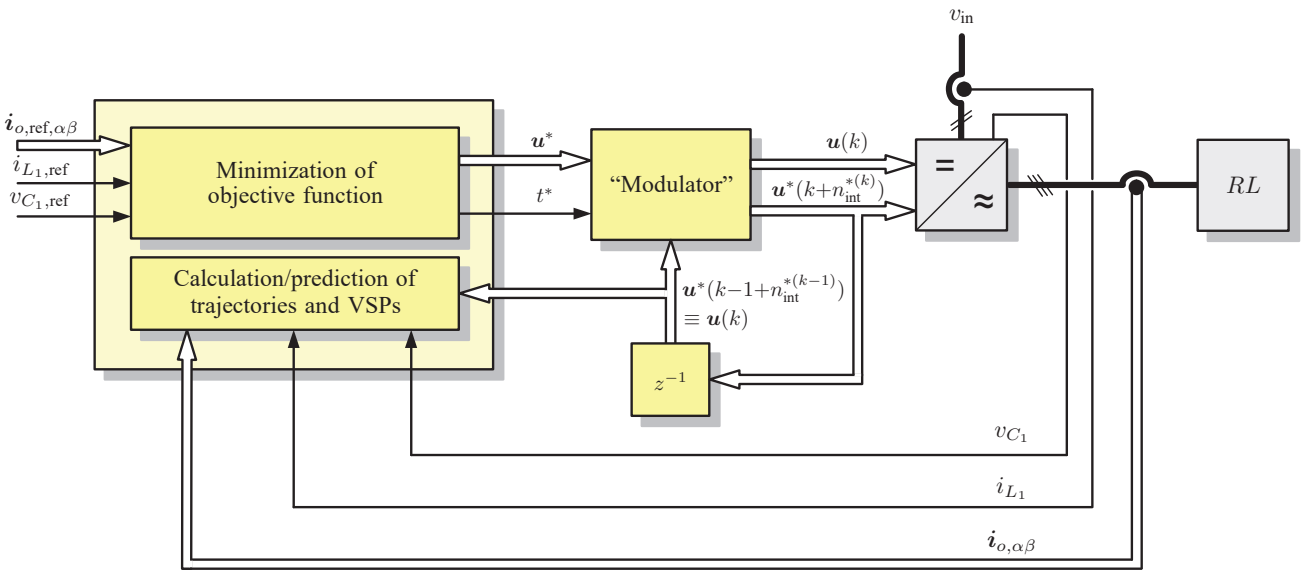

Fig. 5: Variable switching point predictive current control (VP^{2}CC) for the qZSI.

to the converter. To do so, the computed optimal time instant t^* is translated into a feasible[8] switching instant via

$$n_{\text{int}}^* = \left\lceil \frac{t^*}{T_s'} \right\rfloor , \tag{23}$$

where $\lceil \star \rfloor$ denotes rounding to the closest integer. Thus, $\boldsymbol{u}^*$ is applied at time-step $k + n_{\text{int}}^{*(k)}$, or, equivalently, at time-instant $n_{\text{int}}^* T_s'$. This means that the modulator first outputs the previously applied switches position $\boldsymbol{u}^*(k-1+n_{\text{int}}^{*(k-1)}) = \boldsymbol{u}(k)$ until time instant $n_{\text{int}}^* T_s'$. Following, it implements the computed optimal switches position $\boldsymbol{u}^*(k + n_{\text{int}}^{*(k)})$ until the end of the sampling interval T_s. At the next time-step $k+1$, the whole procedure is repeated with new measurements. The block diagram of the proposed VSP^{2}CC for the qZSI is shown in Fig. 5.

IV. Experimental Results

To examine the performance of the proposed VSP^{2}CC strategy for the qZSI configuration, shown in Fig. 1, experiments were conducted in the laboratory. Fig. 6 shows the experimental setup, consisting of a 3 kW variable dc power supply, a 3 kW qZSI prototype and an RL load. The three-phase IGBT bridge Powerex IPM PM300CLA060 module and the RURG3060 diode are used as power switches on the ac and dc side of the converter, respectively. For the implementation of the proposed control algorithm, a low-cost, low-power field programmable logic array (FPGA) Cyclone III-EP3C40Q240C8, with 39,600 logic elements, 126 multipliers, and 1,161,216 total RAM bits is employed[9]. Moreover, for the sake of comparison, the conventional direct MPC is also investigated [24], [47].

To compensate for the time delay introduced by the proposed and conventional direct MPC algorithms, a delay compensation strategy is applied [48]. Concerning the computational demand, VSP^{2}CC needs higher calculation time than the conventional direct MPC. Specifically, the latter is executed in 3μs, while the proposed VSP^{2}CC requires 5μs. By using the aforementioned FPGA, both algorithms can be easily implemented and executed well within the chosen sampling interval mentioned below.

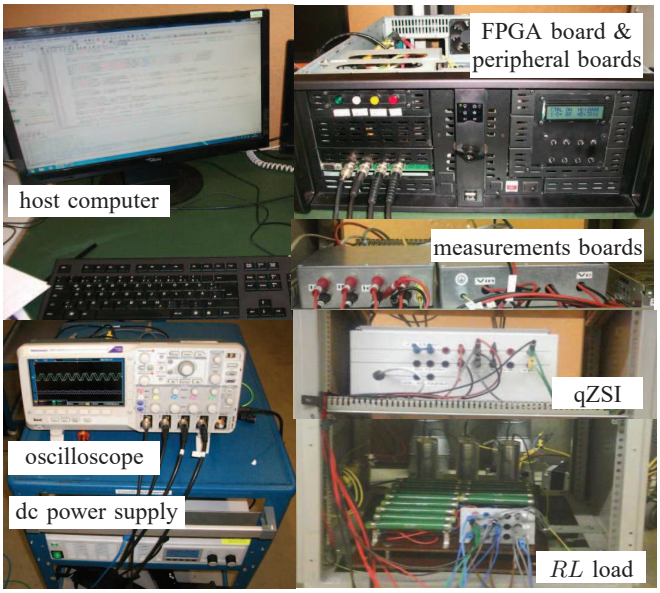

Fig. 6: Experimental setup.

The system parameters are $v_{\text{in}} = 53\,\text{V}$, $L_1 = L_2 = 1\,\text{mH}$, $C_1 = C_2 = 480\,\mu\text{F}$, $R = 10\,\Omega$, and $L = 10\,\text{mH}$. Based on the desired output power ($P_{o,\text{ref}} = 240\,\text{W}$), the output current reference, given by

$$\boldsymbol{i}_{o,\text{ref}} = \sqrt{\frac{2P_{o,\text{ref}}}{3R}} \tag{24}$$

is set to $4\,\text{A}$. As for the inductor current reference, it is computed according to the steady-state power balance, i.e.,,

[8]Given that $t^* \in [0, T_s)$, the VSP needs to be "discretized" on the basis of the sampling interval T_s' of the modulator.

[9]For more details on the setup the reader is referred to [46].

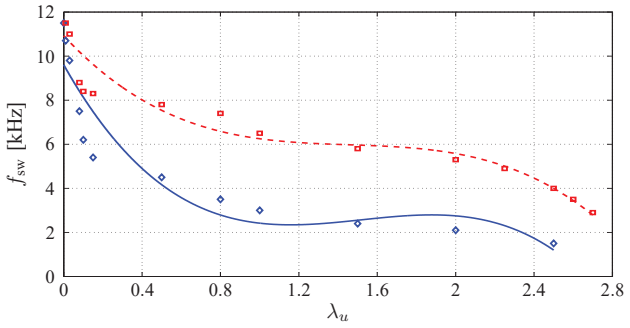

Fig. 7: The effect of the weighting factor λ_u on the switching frequency f_{sw}. The data points were approximated using third-degree polynomials; the solid (blue) line refers to the VSP^{2}CC, and the dashed (red) line to the conventional direct MPC.

$i_{L_1,\text{ref}} = P_{o,\text{ref}}/v_{\text{in}}$. Therefore, it is equal to $\approx 4.5\,\text{A}$. Finally, the capacitor voltage reference $v_{C_1,\text{ref}}$ is derived according to the analysis presented in [24] (see (11)-(12) in Section V). Hence, in order to keep the peak dc-link voltage $\hat{v}_{\text{dc}}$ at 180 V, a capacitor voltage $v_{C_1,\text{ref}} = 120\,\text{V}$ is required.

The sampling interval used for the VSP^{2}CC algorithm and the modulator block is $T_s = 25\,\mu\text{s}$, and $T_s' = 0.25\,\mu\text{s}$, i.e., $m = 100$, receptively. With regards to the choice of the weighting factors in (20), as explained in Section III-B, to achieve accurate tracking of the output current, the latter is prioritized over the tracking of the inductor current and capacitor voltage. This is done by imposing large penalties on the output current error tracking terms in $\boldsymbol{Q}$, i.e., $\boldsymbol{Q} = \text{diag}(1, 1, 0.1, 0.02)$. Keeping the entries of $\boldsymbol{Q}$ fixed, the weighting factor λ_u is adjusted for the converter to operate at the desired switching frequency f_{sw}, as computed by (21). This is done by exploring the trade-off surface [49] of the λ_u–f_{sw} characteristic. This is depicted in Fig. 7 for both the conventional direct MPC and the proposed VSP^{2}CC schemes, where the individual simulations were approximated by a third-order polynomial function.

A. Steady-State Operation

The steady-state performance of the qZSI is examined with the proposed VSP^{2}CC and the conventional direct MPC with prediction horizon of one time step [24], see Figs. 8 and 9, respectively. For both controllers, the average switching frequency is adjusted to $f_{\text{sw}} \approx 3.4\,\text{kHz}$ by setting λ_u in (20) equal to 0.75 and 2.6 for VSP^{2}CC and the conventional direct MPC, respectively.

As can be seen, the dc-side variables effectively track their reference values in both examined cases. Specifically, the capacitor voltages (Figs. 8(a) and 9(a)) and the inductor currents (Figs. 8(b) and 9(b)) are regulated along their references resulting in the desired peak dc-link voltage of 180 V (Figs. 8(c) and 9(c)). Although both controllers introduce zero steady-state error for both dc quantities of concern, VSP^{2}CC produces inductor current of about 50% less ripples than the conventional direct MPC. This results from the fact the shoot-through state can be applied for less than T_s, meaning that the inductor current deviation from its reference can be controlled more effectively.

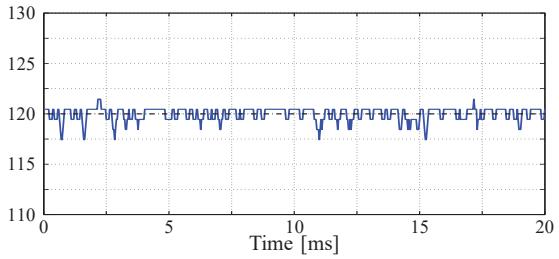

(a) Capacitor voltage v_{C_1} (solid line) and its reference (dash-dotted line) in [V].

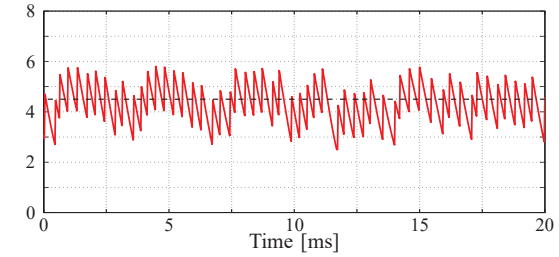

(b) Inductor current i_{L_1} (solid line) and its reference (dash-dotted line) in [A].

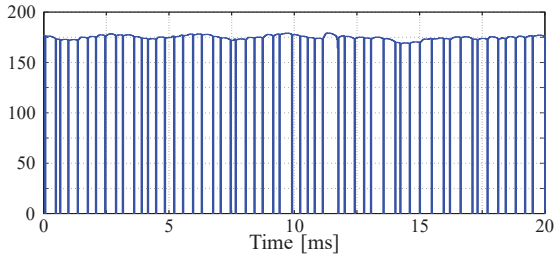

(c) Dc-link voltage v_{dc} in [V].

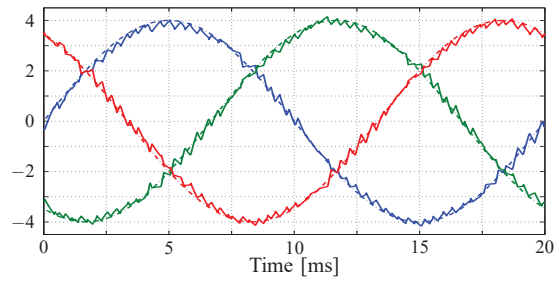

(d) Three-phase output current $\boldsymbol{i}_o$ (solid lines) and their references (dash-dotted lines) in [A].

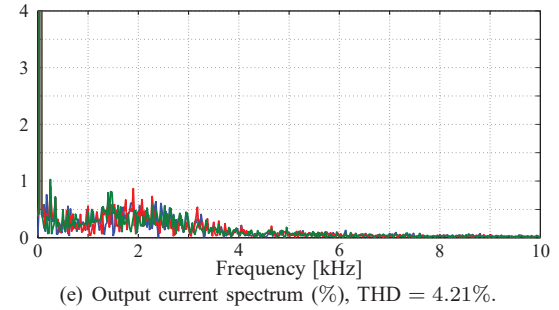

(e) Output current spectrum (%), THD = 4.21%.

Fig. 8: Experimental results of the dc and ac side of the qZSI with the VSP^{2}CC. The sampling interval is $T_s = 25\,\mu\text{s}$ and the switching frequency is $f_{\text{sw}} \approx 3.4\,\text{kHz}$.

With regards to the ac side, Figs. 8(d) and 9(d) show that the output current accurately tracks its reference with

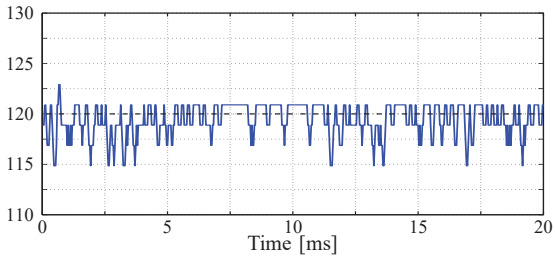

(a) Capacitor voltage v_{C_1} (solid line) and its reference (dash-dotted line) in [V].

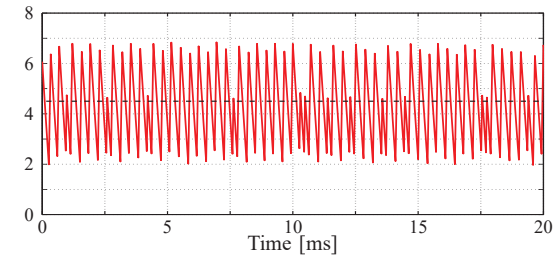

(b) Inductor current i_{L_1} (solid line) and its reference (dash-dotted line) in [A].

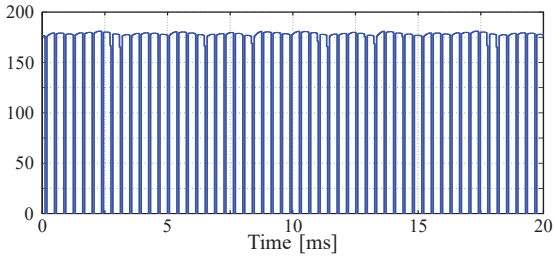

(c) Dc-link voltage v_{dc} in [V].

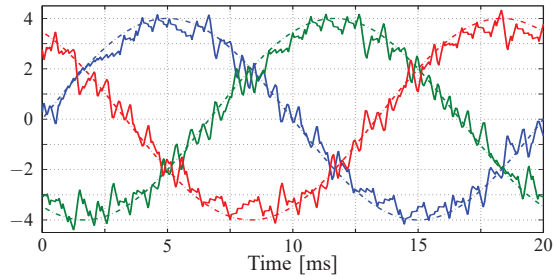

(d) Three-phase output current $\boldsymbol{i}_o$ (solid lines) and their references (dash-dotted lines) in [A].

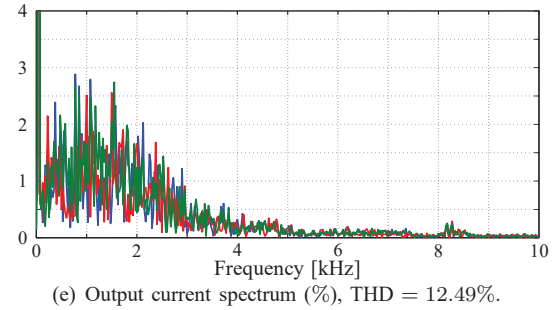

(e) Output current spectrum (%), THD = 12.49%.

Fig. 9: Experimental results of the dc and ac side of the qZSI with the conventional one-step horizon direct MPC [24]. The sampling interval is $T_s = 25\,\mu$s and the switching frequency is $f_{\text{sw}} \approx 3.4\,$kHz.

both control strategies under examination. However, VSP^{2}CC produces currents with 4.21% THD, notably lower than the

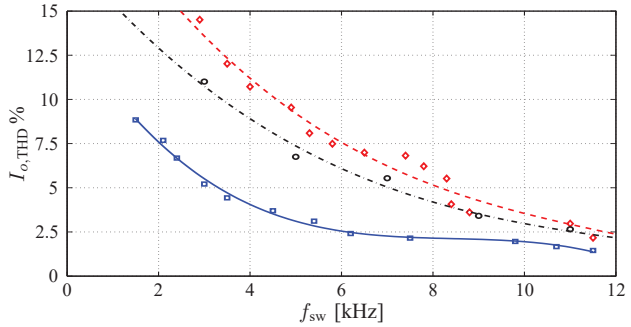

Fig. 10: Trade-off between the current THD $I_{o,\text{THD}}$ and the switching frequency f_{sw}. The individual experimental results were approximated with third-degree polynomials. The solid (blue) line refers to the VSP^{2}CC, the dashed (red) line to the conventional one-step direct MPC, and the dash-dotted (black) line to the linear controller with PWM.

THD the conventional one-step horizon direct MPC produces, i.e., 12.49%, see Figs. 8(e) and 9(e), respectively. Thanks to the introduction of the optimal switching time instant and the additional "modulation" phase, the proposed MPC algorithm applies the switches positions that result in high current ripples for shorter time intervals than the conventional direct MPC does.

Furthermore, the trade-off between the output current THD and the switching frequency of the two discussed MPC schemes is investigated. In this experiment, λ_u is varied to obtain a wide range of switching frequencies, between 1.5 kHz and 12 kHz. The individual results are approximated by a polynomial of third degree and shown in Fig. 10. In the same figure, the THD produced by a PI-based linear controller with a PWM stage is included[10]. As can be observed, the VSP^{2}CC produces lower THD over the whole range of the examined switching frequencies compared with not only the conventional direct MPC, but also the linear controller with PWM. This becomes more prominent for lower switching frequencies. For example, at the lower end of the examined range of switching frequencies (i.e., $f_{\text{sw}} = 1.5\,$kHz), the proposed method produces currents with 8.89% THD, whereas those produced with the conventional one-step horizon direct MPC and the PWM-based linear controller have THD equal to 18.03% and 13.96%, respectively. This characteristic of VSP^{2}CC makes it potentially an attractive option for high power converters, given that these systems need to be operated at low switching frequencies for the switching losses—which typically dominate the conduction losses for such applications—to be kept low.

B. Response During Transients

The transient behavior of the proposed VSP^{2}CC and conventional direct MPC is examined under a step change in the output current reference. More specifically, the desired output power $P_{o,\text{ref}}$ is stepped up from 60 W to 240 W and that change is translated into the corresponding current steady-state references (see (24)). Therefore, the output current is changed from 2 A to 4 A, and the inductor current reference from

[10]For a comprehensive comparison between the conventional one-step and multistep direct MPC and a PI-based controller, the reader is referred to [24].

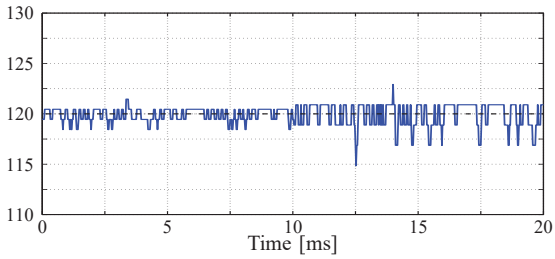

(a) Capacitor voltage v_{C_1} (solid line) and its reference (dash-dotted line) in [V].

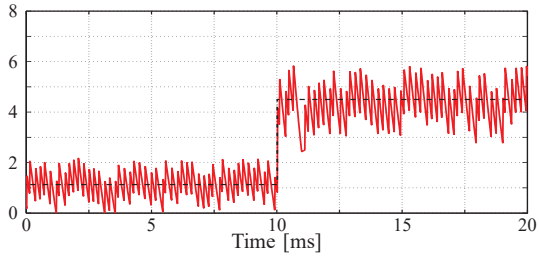

(b) Inductor current i_{L_1} (solid line) and its reference (dash-dotted line) in [A].

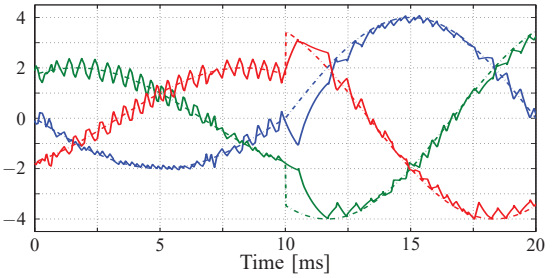

(c) Three-phase output current $\boldsymbol{i}_o$ (solid lines) and their references (dash-dotted lines) in [A].

Fig. 11: Experimental results of the dc and ac side of the qZSI with VSP^{2}CC under a step-up change in the output current reference.

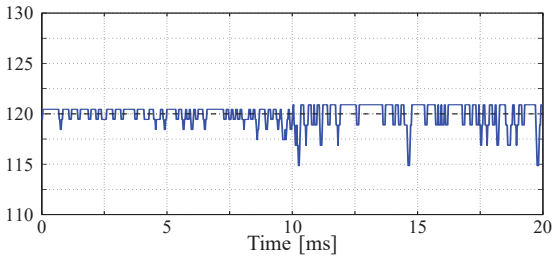

(a) Capacitor voltage v_{C_1} (solid line) and its reference (dash-dotted line) in [V].

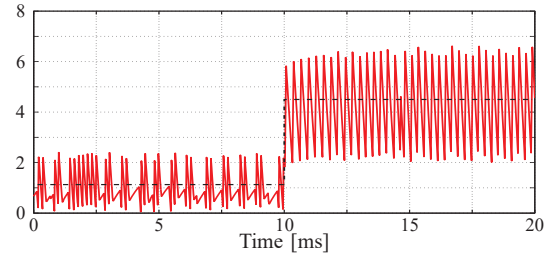

(b) Inductor current i_{L_1} (solid line) and its reference (dash-dotted line) in [A].

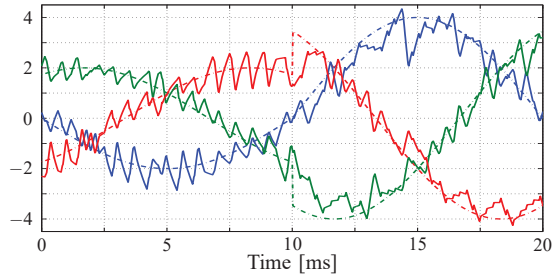

(c) Three-phase output current $\boldsymbol{i}_o$ (solid lines) and their references (dash-dotted lines) in [A].

Fig. 12: Experimental results of the dc and ac side of the qZSI with conventional MPC under a step-up change in the output current reference.

≈ 1.1 A to ≈ 4.5 A. Finally, the capacitor voltage reference is kept fixed at 120 V.

The dc- and ac-side results obtained with VSP^{2}CC and conventional direct MPC are shown in Figs. 11 and 12, respectively. As can be seen in Figs. 11(a) and 12(a), the capacitor voltage remains practically unaffected, with no under- or overshoot observed, regardless of the employed control strategy. As far as the inductor current is concerned, both controllers manage to regulate it along its reference, with zero steady-state error, both before and after the step change (Figs. 11(b) and 12(b)). As can be observed, VSP^{2}CC inherits the fast transient response from the conventional direct MPC. However, it produces lower inductor current ripples at both operating points.

As for the ac-side current, both controllers avoid any steady-state tracking errors, and successfully reach the new desired value of the output current within a short transient response time, see Figs. 11(c) and 12(c). The high dynamic performance that characterizes direct MPC schemes is also observed with VSP^{2}CC. The latter, though, exhibits favorable performance in terms of output current distortion (as quantified by the output current THD, see Fig. 10). As a result, the performance of the converter is considerably improved.

Finally, it is worthwhile to mention that since VSP^{2}CC is a derivative of the conventional direct MPC, it inherits other qualities that characterize such a scheme. Among those, it is robustness to model mismatches and disturbances, as examined in [24, Section V-C]. Owing to the receding horizon policy of MPC—according to which the optimization problem is solved at every time step based on updated measurements [50]—feedback is added to the control scheme, thus ensuring that the controller is robust to modeling errors.

V. Conclusions

This paper presents a variable switching point predictive current control (VSP^{2}CC) for the quasi-Z-source inverter (qZSI). The proposed algorithm controls both sides of the converter, i.e., the output current on the ac side as well as the inductor current and capacitor voltage on the dc side. Having as a goal to reduce the output and inductor current ripples—thus, eventually, to improve the system performance—VSP^{2}CC can apply the (optimal) switches position not only at the discrete time instants, but also at any time instant within the sampling interval. By doing so, the switches position that results in high current ripples (i.e., that position that results in operation at the shoot-through state) can be applied for a

shorter time. Although the presented method is more computationally expensive than a conventional one-step horizon direct model predictive control (MPC) scheme, it can be successfully implemented on a low-cost FPGA. To validate the efficacy of the proposed algorithm, VSP^{2}CC is compared through experiments with its conventional counterpart. As shown, the proposed strategy results in lower inductor current ripples and less output current total harmonic distortion (THD) for a given switching frequency.

APPENDIX

According to the inductor volt-second balance, when the converter operates at steady-state, the average voltage of the inductors is zero over one time window $T_1 = n_1 T_s$, with $n_1 \gg 0, n_1 \in \mathbb{N}^+$, and $T_1 \approx 1/f_{\text{sw}}$, with f_{sw} being the *average* switching frequency, as described by (21).[11] Consequently, the voltages v_{C_1} and v_{C_2} across the capacitors C_1 and C_2, respectively, as well as the currents through the inductors L_1 and L_2, i.e., i_{L_1} and i_{L_2}, respectively, are given by

$$v_{C_1} = \frac{1-d}{1-2d} v_{\text{in}}\,, \quad v_{C_2} = \frac{d}{1-2d} v_{\text{in}}\,, \tag{25a}$$

$$i_{L_1} = i_{L_2} = \frac{1-d}{1-2d} i_{\text{load}}\,, \tag{25b}$$

where it is assumed that $C_1 = C_2$ and $L_1 = L_2$. Moreover, i_{load} is the load current, see Fig. 2(a). In (25), $d \in [0,\ 0.5)$ stands for the *average* shoot-through duty cycle of the qZSI, defined as

$$d = \frac{T_{\text{st}}}{T_1} = \frac{n_{\text{st}} T_s}{n_1 T_s} = \frac{n_{\text{st}}}{n_1}\,, \tag{26}$$

where T_{st} is the shoot-through time interval, i.e., the time interval within the time window T_1 for which the load is short-circuited, and $n_{\text{st}} < \frac{n_1}{2}$, $n_{\text{st}}, n_1 \in \mathbb{N}^+$. Finally, the peak value of the dc-link voltage during the non-shoot-through interval is

$$\hat{v}_{\text{dc}} = v_{C_1} + v_{C_2} = \frac{1}{1-2d} v_{\text{in}}\,. \tag{27}$$

REFERENCES

[1] A. Ayman, P. Karamanakos, and R. Kennel, "Variable switching point predictive current control of quasi-Z-source inverters," in *Proc. App. Power Electron. Conf. and Expo.*, Tampa, FL, Mar. 2017, pp. 2773–2780.

[2] F. Z. Peng, "Z-source inverter," *IEEE Trans. Ind. Appl.*, vol. 39, no. 2, pp. 504–510, Mar./Apr. 2003.

[3] Y. P. Siwakoti, F. Z. Peng, F. Blaabjerg, P. C. Loh, and G. E. Town, "Impedance-source networks for electric power conversion Part I: A topological review," *IEEE Trans. Power Electron.*, vol. 30, no. 2, pp. 699–716, Feb. 2015.

[4] P. C. Loh and F. Blaabjerg, "Magnetically coupled impedance-source inverters," *IEEE Trans. Ind. Appl.*, vol. 49, no. 5, pp. 2177–2187, Sep./Oct. 2013.

[5] Y. Liu, H. Abu-Rub, and B. Ge, "Z-source/quasi-Z-source inverters: Derived networks, modulations, controls, and emerging applications to photovoltaic conversion," *IEEE Ind. Electron. Mag.*, vol. 8, no. 4, pp. 32–44, Dec. 2014.

[6] M. Shen, J. Wang, A. Joseph, F. Z. Peng, L. M. Tolbert, and D. J. Adams, "Constant boost control of the Z-source inverter to minimize current ripple and voltage stress," *IEEE Trans. Ind. Appl.*, vol. 42, no. 3, pp. 770–778, May/Jun. 2006.

[11] With direct MPC, the switching frequency is variable due to the absence of a modulator. Therefore, the operating switching frequency of the converter is indicated by the average switching frequency, see Section III-B.

[7] J. Anderson and F. Peng, "Four quasi-Z-source inverters," in *Proc. IEEE Power Electron. Spec. Conf.*, Rhodes, Greece, Jun. 2008, pp. 2743–2749.

[8] S. Yang, F. Z. Peng, Q. Lei, R. Inoshita, and Z. Qian, "Current-fed quasi-Z-source inverter with voltage buck-boost and regeneration capability," *IEEE Trans. Ind. Appl.*, vol. 47, no. 2, pp. 882–892, Mar./Apr. 2011.

[9] F. Guo, L. X. Fu, C. H. Lin, C. Li, W. Choi, and J. Wang, "Development of an 85 kW bidirectional quasi-Z-source inverter with dc-link feedforward compensation for electric vehicle applications," *IEEE Trans. Power Electron.*, vol. 28, no. 12, pp. 5477–5488, Dec. 2013.

[10] A. Battiston, E.-H. Miliani, S. Pierfederici, and F. Meibody-Tabar, "Efficiency improvement of a quasi-Z-source inverter-fed permanent-magnet synchronous machine-based electric vehicle," *IEEE Trans. Transport. Electrif.*, vol. 2, no. 1, pp. 14–23, Mar. 2016.

[11] Y. Li, S. Jiang, J. G. Cintron-Rivera, and F. Z. Peng, "Modeling and control of quasi-Z-source inverter for distributed generation applications," *IEEE Trans. Ind. Electron.*, vol. 60, no. 4, pp. 1532–1541, Apr. 2013.

[12] J. Liu, S. Jiang, D. Cao, and F. Z. Peng, "A digital current control of quasi-Z-source inverter with battery," *IEEE Trans. Ind. Informat.*, vol. 9, no. 2, pp. 928–937, May 2013.

[13] B. Ge, H. Abu-Rub, F. Z. Peng, Q. Lei, A. T. de Almeida, F. J. T. E. Ferreira, D. Sun, and Y. Liu, "An energy-stored quasi-Z-source inverter for application to photovoltaic power system," *IEEE Trans. Ind. Electron.*, vol. 60, no. 10, pp. 4468–4481, Oct. 2013.

[14] A. Ayad, S. Hanafiah, and R. Kennel, "A comparison of quasi-Z-source inverter and traditional two-stage inverter for photovoltaic application," in *Proc. Int. Exhib. and Conf. for Power Electron., Intell. Motion, Renew. Energy and Energy Manag.*, Nuremberg, Germany, May 2015, pp. 1–8.

[15] Q. Lei, F. Z. Peng, and B. Ge, "Transient modeling of current-fed quasi-Z-source inverter," in *Proc. IEEE Energy Convers. Congr. Expo.*, Phoenix, AZ, Sep. 2011, pp. 2283–2287.

[16] Y. P. Siwakoti, F. Z. Peng, F. Blaabjerg, P. C. Loh, and G. E. Town, "Impedance-source networks for electric power conversion Part II: Review of control and modulation techniques," *IEEE Trans. Power Electron.*, vol. 30, no. 4, pp. 1887–1906, Apr. 2015.

[17] O. Ellabban, M. Mosa, H. Abu-Rub, and J. Rodríguez, "Model predictive control of a grid connected quasi-Z-source inverter," in *Proc. IEEE Int. Conf. Ind. Technol.*, Cape Town, South Africa, Feb. 2013, pp. 1591–1596.

[18] M. Mosa, G. M. Dousoky, and H. Abu-Rub, "A novel FPGA implementation of a model predictive controller for SiC-based quasi-Z-source inverters," in *Proc. App. Power Electron. Conf. and Expo.*, Fort Worth, TX, Mar. 2014, pp. 1293–1298.

[19] S. Bayhan, H. Abu-Rub, and R. S. Balog, "Model predictive control of quasi-Z-source four-leg inverter," *IEEE Trans. Ind. Electron.*, vol. 63, no. 7, pp. 4506–4516, Jul. 2016.

[20] A. Bakeer, M. Ismeil, and M. Orabi, "A powerful finite control set-model predictive control algorithm for quasi Z-source inverter," *IEEE Trans. Ind. Informat.*, vol. 12, no. 4, pp. 1371–1379, Aug. 2016.

[21] Y. Liu, B. Ge, H. Abu-Rub, H. Sun, F. Z. Peng, and Y. Xue, "Model predictive direct power control for active power decoupled single-phase quasi-Z-source inverter," *IEEE Trans. Ind. Informat.*, vol. 12, no. 4, pp. 1550–1559, Aug. 2016.

[22] A. Ayad, P. Karamanakos, and R. Kennel, "Direct model predictive voltage control of quasi-Z-source inverters with *LC* filters," in *Proc. Eur. Power Electron. Conf.*, Karlsruhe, Germany, Sep. 2016, pp. 1–10.

[23] M. Mosa, R. S. Balog, and H. Abu-Rub, "High performance predictive control of quasi impedance source inverter," *IEEE Trans. Power Electron.*, vol. 32, no. 4, pp. 3251–3262, Apr. 2017.

[24] A. Ayman, P. Karamanakos, and R. Kennel, "Direct model predictive current control strategy of quasi-Z-source inverters," *IEEE Trans. Power Electron.*, vol. 32, no. 7, pp. 5786–5801, Jul. 2017.

[25] P. Cortés, M. P. Kazmierkowski, R. M. Kennel, D. E. Quevedo, and J. Rodríguez, "Predictive control in power electronics and drives," *IEEE Trans. Ind. Electron.*, vol. 55, no. 12, pp. 4312–4324, Dec. 2008.

[26] T. Geyer, "A comparison of control and modulation schemes for medium-voltage drives: Emerging predictive control concepts versus PWM-based schemes," *IEEE Trans. Ind. Appl.*, vol. 47, no. 3, pp. 1380–1389, May/Jun. 2011.

[27] T. Geyer, N. Oikonomou, G. Papafotiou, and F. D. Kieferndorf, "Model predictive pulse pattern control," *IEEE Trans. Ind. Appl.*, vol. 48, no. 2, pp. 663–676, Mar./Apr. 2012.

[28] N. Oikonomou, C. Gutscher, P. Karamanakos, F. D. Kieferndorf, and T. Geyer, "Model predictive pulse pattern control for the five-level active neutral point clamped inverter," *IEEE Trans. Ind. Appl.*, vol. 49, no. 6, pp. 2583–2592, Nov./Dec. 2013.

[29] S. Vazquez, J. I. Leon, L. G. Franquelo, J. Rodríguez, H. A. Young, A. Marquez, and P. Zanchetta, "Model predictive control: A review of

its applications in power electronics," *IEEE Ind. Electron. Mag.*, vol. 8, no. 1, pp. 16–31, Mar. 2014.
[30] P. Karamanakos, T. Geyer, N. Oikonomou, F. D. Kieferndorf, and S. Manias, "Direct model predictive control: A review of strategies that achieve long prediction intervals for power electronics," *IEEE Ind. Electron. Mag.*, vol. 8, no. 1, pp. 32–43, Mar. 2014.
[31] Y. Zhang, H. Yang, and B. Xia, "Model-predictive control of induction motor drives: Torque control versus flux control," *IEEE Trans. Ind. Appl.*, vol. 52, no. 5, pp. 4050–4060, Sep./Oct. 2016.
[32] T. Geyer, *Model predictive control of high power converters and industrial drives*. Hoboken, NJ: Wiley, 2016.
[33] S. Vazquez, J. Rodríguez, M. Rivera, L. G. Franquelo, and M. Norambuena, "Model predictive control for power converters and drives: Advances and trends," *IEEE Trans. Ind. Electron.*, vol. 64, no. 2, pp. 935–947, Feb. 2017.
[34] Y. Zhang, W. Xie, Z. Li, and Y. Zhang, "Model predictive direct power control of a PWM rectifier with duty cycle optimization," *IEEE Trans. Power Electron.*, vol. 28, no. 11, pp. 5343–5351, Nov. 2013.
[35] P. Karamanakos, P. Stolze, R. M. Kennel, S. Manias, and H. du Toit Mouton, "Variable switching point predictive torque control of induction machines," *IEEE J. Emerg. Sel. Topics Power Electron.*, vol. 2, no. 2, pp. 285–295, Jun. 2014.
[36] L. Tarisciotti, P. Zanchetta, A. Watson, S. Bifaretti, and J. C. Clare, "Modulated model predictive control for a seven-level cascaded H-bridge back-to-back converter," *IEEE Trans. Ind. Electron.*, vol. 61, no. 10, pp. 5375–5383, Oct. 2014.
[37] L. Tarisciotti, P. Zanchetta, A. Watson, J. C. Clare, M. Degano, and S. Bifaretti, "Modulated model predictive control for a three-phase active rectifier," *IEEE Trans. Ind. Appl.*, vol. 51, no. 2, pp. 1610–1620, Mar./Apr. 2015.
[38] P. Stolze, P. Karamanakos, R. Kennel, S. Manias, and C. Endisch, "Effective variable switching point predictive current control for ac low-voltage drives," *Int. J. of Control*, vol. 88, no. 7, pp. 1366–1378, Jul. 2015.
[39] Q. Liu and K. Hameyer, "Torque ripple minimization for direct torque control of PMSM with modified FCSMPC," *IEEE Trans. Ind. Appl.*, vol. 52, no. 6, pp. 4855–4864, Nov./Dec. 2016.
[40] Y. Zhang, Y. Peng, and C. Qu, "Model predictive control and direct power control for PWM rectifiers with active power ripple minimization," *IEEE Trans. Ind. Appl.*, vol. 52, no. 6, pp. 4909–4918, Nov./Dec. 2016.
[41] L. Tarisciotti, A. Formentini, A. Gaeta, M. Degano, P. Zanchetta, R. Rabbeni, and M. Pucci, "Model predictive control for shunt active filters with fixed switching frequency," *IEEE Trans. Ind. Appl.*, vol. 53, no. 1, pp. 296–304, Jan./Feb. 2017.
[42] M. Vijayagopal, P. Zanchetta, L. Empringham, L. de Lillo, L. Tarisciotti, and P. Wheeler, "Control of a direct matrix converter with modulated model-predictive control," *IEEE Trans. Ind. Appl.*, vol. 53, no. 3, pp. 2342–2349, May/Jun. 2017.
[43] Y. Zhang, D. Xu, J. Liu, S. Gao, and W. Xu, "Performance improvement of model-predictive current control of permanent magnet synchronous motor drives," *IEEE Trans. Ind. Appl.*, vol. 53, no. 4, pp. 3683–3695, Jul./Aug. 2017.
[44] L. Tarisciotti, J. Lei, A. Formentini, A. Trentin, P. Zanchetta, P. Wheeler, and M. Rivera, "Modulated predictive control for indirect matrix converter," *IEEE Trans. Ind. Appl.*, vol. 53, no. 5, pp. 4644–4654, Sep./Oct. 2017.
[45] S. N. Manias, *Power electronics and motor drive systems*. Cambridge, MA: Academic Press, 2016.
[46] A. N. F. Ayad, "Advanced control techniques of impedance source inverters for distributed generation applications," Ph.D. dissertation, Chair of Elect. Drive Syst. and Power Electron. TU München, Munich, Germany, 2017.
[47] A. Ayad and R. Kennel, "Direct model predictive control of quasi-Z-source inverter compared with the traditional PI-based PWM control," in *Proc. Eur. Power Electron. Conf.*, Geneva, Switzerland, Sep. 2015, pp. 1–9.
[48] P. Cortés, J. Rodríguez, C. Silva, and A. Flores, "Delay compensation in model predictive current control of a three-phase inverter," *IEEE Trans. Ind. Electron.*, vol. 59, no. 2, pp. 1323–1325, Feb. 2012.
[49] S. Boyd and L. Vandenberghe, *Convex Optimization*. Cambridge, UK: Cambridge Univ. Press, 2004.
[50] J. B. Rawlings and D. Q. Mayne, *Model Predictive Control: Theory and Design*. Madison, WI: Nob Hill, 2009.

Petros Karamanakos (S'10–M'14) received the Diploma and the Ph.D. degrees in electrical and computer engineering from the National Technical University of Athens (NTUA), Athens, Greece, in 2007, and 2013, respectively.

From 2010 to 2011 he was with the ABB Corporate Research Center, Baden-Dättwil, Switzerland, where he worked on model predictive control strategies for medium-voltage drives. From 2013 to 2016 he was a PostDoc Research Associate in the Chair of Electrical Drive Systems and Power Electronics, Technische Universität München, Munich, Germany. He is currently an Assistant Professor in the Faculty of Computing and Electrical Engineering, Tampere University of Technology, Tampere, Finland. His main research interests lie at the intersection of optimal control, mathematical programming and power electronics, including model predictive control for power electronic converters and ac drives.

Dr. Karamanakos received the 2014 Third Best Paper Award of the IEEE Transactions on Industry Applications and the First Prize Paper Award of the Industrial Drives Committee at the 2013 IEEE Energy Conversion Congress and Exposition.

Ayman Ayad (S'13–M'17) received the B.Sc. degree in electronic engineering and the M.Sc. degree in automatic control from Menofia University, Menofia and Cairo University, Giza, Egypt, in 2006 and 2009, respectively. In July 2017, he got his Ph.D. degree from the Chair of Electrical Drive Systems and Power Electronics, Technische Universität München, Munich, Germany.

From 2007 to 2011, he was a teaching assistant in the department of Electrical and Computer Engineering, Sinai University, Al-Arish, North Sinai, Egypt. He is currently working as a development and system engineer in the powertrain department, Continental Automotive GmbH, Regensburg, Germany. His research interests include power electronic converters, model predictive control, electric machines, electric vehicles, and renewable energy systems.

Ralph Kennel (M'89–SM'96) received the Diploma and Dr.-Ing. (Ph.D.) degrees from the University of Kaiserslautern, Kaiserslautern, Germany, in 1979 and 1984, respectively.

From 1983 to 1999 he worked on several positions with Robert BOSCH GmbH, Germany. Until 1997, he was responsible for the development of servo drives. He was one of the main supporters of VECON and SERCOS interface, two multicompany development projects for a microcontroller and a digital interface especially dedicated to servo drives. Furthermore, he actively took part in the definition and release of new standards with respect to CE marking for servo drives. Between 1997 and 1999, he was responsible for "Advanced and Product Development of Fractional Horsepower Motors" in automotive applications. His main activity was preparing the introduction of brushless drive concepts to the automotive market. From 1994 to 1999, he was appointed Visiting Professor at the Newcastle University, Newcastle-upon-Tyne, U.K. From 1999 to 2008, he was Professor for Electrical Machines and Drives at Wuppertal University, Wuppertal, Germany. Since 2008 he is Professor for Electrical Drive Systems and Power Electronics at Technische Universtät München, Munich, Germany. His main interests today are sensorless control of ac drives, predictive control of power electronics and hardware-in-the-loop systems.

Dr. Kennel is a Senior Member of IEEE, a Fellow of IEE and a Chartered Engineer in the U.K. Within IEEE, he is Treasurer of the Germany Section as well as ECCE Global Partnership Chair of the Power Electronics Society (PELS). Dr. Kennel has received in 2013 the Harry Owen Distinguished Service Award from IEEE-PELS as well as the EPE Association Distinguished Service Award in 2015. Dr. Kennel was appointed "Extraordinary Professor" by the University of Stellenbosch (South Africa) from 2016 to 2019 and as "Visiting Professor" at the Haixi Institute by the Chinese Academy of Sciences from 2016 to 2021. There he was appointed as "Jiaxi Lu Overseas Guest Professor" in 2017.